



**HAL**  
open science

# Experimental and Numerical Investigation of a Direct Injection Spark Ignition Hydrogen Engine for Heavy-Duty Applications

G. Maio, A. Boberic, L. Giarracca, D. Aubagnac-Karkar, O. Colin, F. Duffour, K. Deppenkemper, L. Virnich, S. Pischinger

► **To cite this version:**

G. Maio, A. Boberic, L. Giarracca, D. Aubagnac-Karkar, O. Colin, et al.. Experimental and Numerical Investigation of a Direct Injection Spark Ignition Hydrogen Engine for Heavy-Duty Applications. *International Journal of Hydrogen Energy*, 2022, 47 (67), pp.29069-29084. 10.1016/j.ijhydene.2022.06.184 . hal-03853877

**HAL Id: hal-03853877**

**<https://ifp.hal.science/hal-03853877>**

Submitted on 15 Nov 2022

**HAL** is a multi-disciplinary open access archive for the deposit and dissemination of scientific research documents, whether they are published or not. The documents may come from teaching and research institutions in France or abroad, or from public or private research centers.

L'archive ouverte pluridisciplinaire **HAL**, est destinée au dépôt et à la diffusion de documents scientifiques de niveau recherche, publiés ou non, émanant des établissements d'enseignement et de recherche français ou étrangers, des laboratoires publics ou privés.

# Experimental and Numerical Investigation of a Direct Injection Spark Ignition Hydrogen Engine for Heavy-Duty Applications

G. Maio<sup>a,\*</sup>, A. Boberic<sup>b,\*\*</sup>, L. Giarracca<sup>a</sup>, D. Aubagnac-Karkar<sup>a</sup>, O. Colin<sup>a</sup>, F. Duffour<sup>a</sup>, K. Deppenkemper<sup>c</sup>, L. Virnich<sup>c</sup>, S. Pischinger<sup>b</sup>

<sup>a</sup>*IFP Energies nouvelles, 1 et 4 avenue de Bois-Préau, 92852 Rueil-Malmaison, France; Institut Carnot IFPEN Transports*

<sup>b</sup>*Chair of Thermodynamics of Mobile Energy Conversion Systems - RWTH Aachen, Forckenbeckstr. 4, 52074 Aachen, Germany*

<sup>c</sup>*FEV Europe GmbH, Neuenhofstr. 181, 52078 Aachen. Germany*

---

## Abstract

The H<sub>2</sub> internal combustion engine is gaining increasing interest especially for commercial vehicles. Regarding the optimization of the combustion process, results of experimental investigations on a H<sub>2</sub> heavy-duty single-cylinder engine in combination with numerical 3D-CFD investigations are presented. In addition to a Direct Injection (DI) Spark Ignited (SI) configuration, Port Fuel Injection (PFI) is explored to provide a reference with near homogeneous cylinder charge. The main objective is to assess a 3D-CFD-RANS framework based on ECFM and state-of-the art sub-models to describe the most important phenomena occurring in H<sub>2</sub> spark ignition engines and to support the experimental analysis. Experimental results show that the PFI configuration provides efficiency and emissions benefits at the expense of volumetric efficiency. The proposed CFD model demonstrates the ability to successfully simulate different engine operating conditions for both PFI and DI systems. In particular, it is shown that the charge stratification typical for DI systems is not beneficial for the studied configuration as it increases wall heat losses and NO<sub>x</sub> formation.

*Keywords:* hydrogen, spark ignition engines, turbulent combustion modeling

---

\*Corresponding author for the numerical part. Email: giampaolo.maio@ifpen.fr

\*\*Corresponding author for the experimental part. Email: boberic@tme.rwth-aachen.de

---

## 1. Introduction

The idea of using hydrogen as a spark ignition engine fuel was already proposed decades ago [1]. However, in the past, technical and economical limitations for its production, transportation and utilization have strongly restricted its use. Nowadays, the urgent need to decarbonize the energy sector together with the progress in hydrogen production have led to renewed interest in H<sub>2</sub> power-train technologies [2]. In particular, the increase in efficiency of the electrolysis process to produce *green* H<sub>2</sub> [3, 4, 5], the possibility to produce *blue* H<sub>2</sub> [6, 7] through carbon capture and storage (CCS) makes its use economically and technically attractive for the near-future [8, 9]. Hence, the European Union formulated a strategy to integrate hydrogen as an energy carrier and increase the penetration of H<sub>2</sub> in the transport sector [10]. On the utilization side, one possibility is to use H<sub>2</sub> in fuel cells [11, 12, 13] and the other is to employ piston spark ignition engines [14]. This latter solution uses an already viable and consolidated technology and it has the advantage of a lower cost and to be less demanding of raw materials and rare-earth-elements compared to fuel cells [15, 16]. These reasons, coupled with the higher volumetric power density compared to electric vehicles, make hydrogen spark ignition engines attractive especially for heavy-duty applications [17, 12]. Together with the advantage of being a carbon-free fuel, hydrogen has also several properties that can potentially lead to an increase of the engine thermodynamic efficiency. The wide flammability limit, combined with the high flame speed compared to gasoline or methane makes diluted lean-operating conditions attractive [18]. However, due to the displacement of the intake air through the low density hydrogen fuel in a PFI configuration, the volumetric efficiency drops considerably [19]. This, coupled with the possibility of backfire makes DI operation a more attractive solution.

The CO<sub>2</sub>, CO and HC emissions from H<sub>2</sub> combustion are zero. However, nitrogen oxide (NO<sub>x</sub>) emissions are still an issue that need to be tackled as

30 their formation strongly depends on the in-cylinder mixture and temperature distribution. To achieve the optimal design of internal combustion engines, work on combined experimental and numerical research studies is an effective and powerful strategy already demonstrated in several literature studies involving also gaseous fuel blends [20, 21]. Recently, numerical simulation has also been  
35 used to investigate the possibility to use pure H<sub>2</sub> for compression ignition engines [22] but without comparing numerical results with an experimental test bench data.

In the present work an integrated numerical and experimental study on a heavy-duty H<sub>2</sub> engine is presented. For this purpose, a single-cylinder engine  
40 of the heavy-duty 13 l six-cylinder engine class has been modified to enable operation with H<sub>2</sub>. The engine configuration made it possible to employ both a PFI and DI injection strategy for a direct comparison. As mixture homogeneity plays an important role for both engine performance and emissions, the PFI configuration will be used as a near-homogeneous reference for the numerical  
45 study. Additionally, this comparison will highlight the potential of DI hydrogen engines in regard to the optimization of the mixture homogenization. In the past, the substitution of natural gas (NG) with H<sub>2</sub> in HD engines to decrease carbon emissions has already been thoroughly investigated. Certain benefits, e.g. improvements in lean burn capabilities from hydrogen shares of up to 40 %  
50 were demonstrated. However, the reduction of the methane number and the volumetric heating value with higher H<sub>2</sub> shares makes a monovalent hydrogen operation unfavorable with conventional NG engines as the high compression ratios will require a de-rating of the engine [23, 24]. In this work, the components for the HD engine were therefore chosen to better support H<sub>2</sub> operation. For  
55 those applications, lean-burn operating strategies show benefits in efficiency and emissions when using 100 % H<sub>2</sub>. Additionally, stoichiometric operation is limited by knocking and is therefore more suited for passenger car applications, considering the lower boost pressure demand is more advantageous for dynamic operation [25, 26].

60 The Extended Coherent Flame Model (ECFM) in both its Reynolds-averaged

Navier-Stokes (RANS) [27] and its large eddy simulation (LES) [28] formulation has demonstrated to be a well suited turbulent combustion model to compute spark-ignition engines [29, 30] accounting for several complex phenomena: ignition [31], flame propagation [27], auto-ignition [32] and pollutant formation [33].  
65 In this work, for the first time, ECFM-RANS is coupled with the CONVERGE CFD solver to model a pure H<sub>2</sub> fueled spark ignition engine. Compared with a previous literature work [34], three dedicated sub-models are introduced to improve the comprehensiveness of the framework:

- a dedicated model for auto-ignition to predict knocking tendencies
- 70 • a burnt-gases NO<sub>x</sub> model based on detailed kinetics
- the Adaptive Mesh Refinement (AMR)

To make the CFD study systematic and complementary to the experimental one, the following stepwise strategy is used:

- As a first step, the CFD model is validated in PFI conditions to avoid any  
75 possible errors coming from mixing mispredictions on an experimental spark advance sweep and on an equivalence ratio variation. Particular focus is put on knocking tendencies and NO<sub>x</sub> formation.
- Then, aware of its potentiality and limitations, the CFD model is used to compute direct injection operating conditions (DI) to improve the understanding of in-cylinder phenomena.  
80

The CFD numerical RANS model based on ECFM-TKI turbulent combustion description will be helpful to explain the observation made on efficiency comparison coming from the experimental part and to derive conclusions on the optimization of the engine design. Furthermore, based on the obtained numerical results, the future challenges for improving CFD modeling of H<sub>2</sub> spark  
85 ignition engines are discussed.

## 2. Experimental setup and measurements

### 2.1. Test bench configuration

The investigations were performed on a 2.13 l heavy-duty single-cylinder  
90 engine. An overview of the test bench setup can be found in Fig. 1. The test  
bench is equipped with an external compressor unit which is able to provide a  
maximum boost pressure ( $p_2$ ) of up to 8 bar. On the other hand, the back-  
pressure on the exhaust side ( $p_5$ ) is governed with an exhaust throttle. The  
intake air temperature is governed by a water-air charge air conditioning system  
95 which is controlled by the test bench management system. A throttle valve  
was installed in the intake side to allow for throttled operation. The engine is  
equipped with a cooled high-pressure EGR, though it was not used in this work.  
A *dSpace* Rapid Control Prototyping Engine Control Unit (ECU) was used for  
the electrical control of the injector and spark plug. The engine coolant and  
100 oil temperature and pressure were managed by external conditioning systems.  
For all measurements, those temperatures were set to 90 °C. The indicated  
pressure data was processed by a FEVIS indication system by *FEV*. For the  
pressure measurement, two low-pressure transducers (max. 10 bar) in the intake  
and exhaust manifold as well as a high-pressure transducer (max. 250 bar) in  
105 the cylinder by Kistler were used. These transducers record 200 engine cycles  
for every measurement with a resolution of 0.1 crank angle degrees (CAD).  
Burn durations and knock parameters were calculated on-line by the indication  
system. The on-line burn function calculation of the indication system uses  
simplified wall heat transfer models optimized for gasoline engines to reduce  
110 computing efforts. The depicted burn rates were therefore recalculated with  
*GT-Power* using three pressure analysis (TPA) for improved accuracy. In Fig.  
2 a comparison of the burn function points of 10 %, 50 % and 90 % mass  
fraction burnt of a collection of various measurements under different operating  
conditions is displayed. The diagram shows that the FEVIS system tends to  
115 overestimate the 10 % and 50 % points.

For the engine investigations, pressurized hydrogen with 300 bar initial pres-

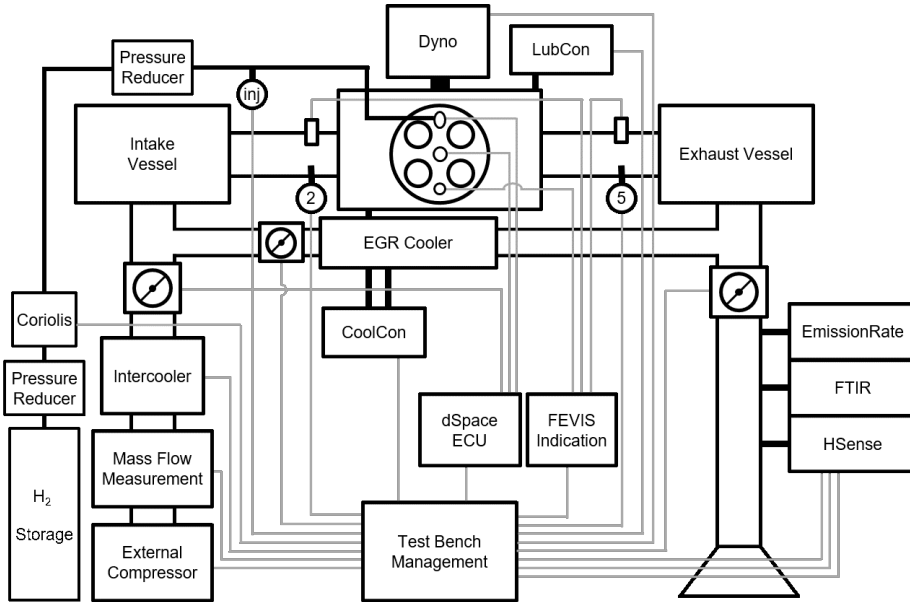


Figure 1: Schematic of the single-cylinder engine test bench.

120 pure and over 99.999 % purity was used. A two-stage pressure regulation system was utilized to achieve a constant operating pressure ( $p_{inj}$ ) of 15 bar at the injector inlet. In between the two pressure regulators a Coriolis mass flow meter was mounted to measure the mean fuel mass flow. A prototype  $H_2$  DI injector was used. Optimization of the mixture formation in this engine is currently ongoing.

125 The chemical properties of hydrogen raise concerns regarding safe operation of the engine test bench. Especially the wide flammability limits in air and the low minimum ignition energy (MIE) pose a challenge [35]. Therefore, several safety precautions were taken. First, multiple hydrogen sensors were mounted throughout the test cell. The detection of hydrogen concentrations of 1 vol-% leads to an immediate engine and fuel line shut-off. This boundary of 25 % of the lower flammability limit is common practice for hydrogen applications [18].

130 Test cell ventilation allows for a continuous dispersion of  $H_2$  leakages in the test cell to keep the concentration beneath the flammability limit. Additionally, several pressure relief valves were mounted in locations where hydrogen could

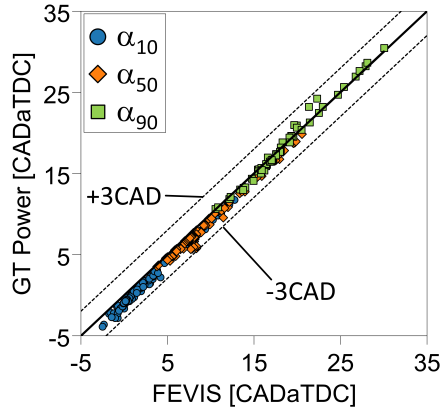


Figure 2: Comparison of the crank angle  $\alpha$  at 10%/50%/90% fuel mass fraction burnt calculated by the FEVIS indication system and GT-Power TPA

accumulate.

The exhaust emissions were analyzed with an emission rate FEVER system by FEV. The system includes a paramagnetic oxygen sensor, while NOx emissions are measured using a chemiluminescence analyzer. The system is also capable of measuring CO<sub>2</sub>, CO and HC emissions. Although those components can result from burning oil, the concentrations are very low and will therefore not be considered in this work. As soot formation from oil burning in the investigated operating point is marginal, no soot measurement equipment was used. Furthermore, a HSense mass spectrometer by *ms4 Analysetechnik* was used to determine the hydrogen concentration in the exhaust gas. This allows for the assessment of the unburnt fuel fraction. Additionally, a FEVER FTIR by FEV was used to determine the humidity of the exhaust gas and verify the NOx concentration.

## 2.2. Combustion system and modifications for H<sub>2</sub> operation

In this work, two hydrogen combustion systems have been studied. A low-pressure DI as well as a PFI configuration to provide a baseline for comparison. A schematic of the setup for both combustion systems is depicted in Fig. 3. As the engine is based on a diesel engine with a flat roof combustion chamber,

modifications had to be made to enable  $H_2$  DI operation. Mainly, the cylinder head was adapted to enable the simultaneous utilization of an injector and spark plug. Therefore, the diesel injector sleeve was replaced with a spark plug sleeve and a lateral, angled bore was used for the injector. For PFI operation, the lateral bore in the cylinder head was closed with a plug and the injector was inserted in the intake runner. A cold-rated racing spark-plug without noble metal electrodes was used. These offer high heat transfer from the electrodes and have no catalytic reaction with  $H_2$ . Consequently, the risk of pre-ignition is lowered by keeping a lower surface temperature. In addition to the aforementioned cylinder head redesign, the piston design had to be revised to achieve a lower compression ratio. Hence, a compact deep piston bowl design was used to reach a geometric compression ratio of 12:1. The valve timings were adapted from the diesel engine to provide maximum cylinder filling.

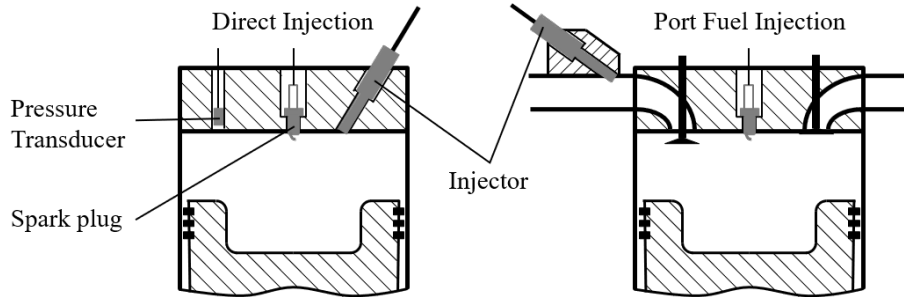


Figure 3: Investigated combustion system layouts.

### 2.3. Measurements

For this work, two parameter variations were investigated. Firstly, a variation of the Air/Fuel ratio (AFR) was performed on the test bench. Then, an ignition sweep was measured. Those two variations allow for a basic characterization of the engine behaviour and are therefore used as a base for the following numerical calculations. The exhaust back-pressure  $p_5$  was controlled to be equal to the intake pressure  $p_2$  as a turbocharger calculation would be needed to determine realistic scavenging pressures. Both variations were per-

formed at  $n = 1200 \text{ min}^{-1}$  and  $IMEP = 10.6 \text{ bar}$ , which is equivalent to the diesel engines cruise point for highway operation. It has a major share in the global operation of a long-haul truck. Hence, optimizing this operating point can influence the overall fuel consumption of the engine significantly [36]. The start of energizing (SOE) for the injector for all DI measurements was set to 180 CAD before top dead center (bTDC) as the intake valve closes (IVC) shortly after at 170 CADbTDC. On the other hand, the PFI injection timing was set to 300 CADbTDC. A late injection into the intake stroke was chosen to reduce the probability of backfire. An overview of the conducted measurements is given in Tab. 1 In post-processing, the fuel consumption and NOx emissions were translated into full scale engine equivalent values.

Table 1: Test matrix of the conducted experimental investigations showing the performed AFR variations (AFRV) and ignition sweeps (IS)

Test	N [rpm]	IMEP [bar]	AFR [-]	COC [CADaTDC]	SOE [CADbTDC]
PFI-AFRV	1200	10.6	1.8 - 2.8	7	300
DI-AFRV	1200	10.6	2.0 - 2.8	7	180
PFI-IS	1200	10.6	2.4	5 - 20	300
DI-IS	1200	10.6	2.4	5 - 19	180

*AFR variation.* As the flammability limits of  $\text{H}_2$  are especially wide, the investigation of the effect of the AFR on combustion is crucial for the operation of a lean-burn  $\text{H}_2$  engine. For both PFI and DI operation, the spark timing was adjusted so the center of combustion (COC) is kept at a constant value of 7 CADaTDC to achieve close to optimal efficiency. The results of the investigation have been summarized in Fig. 4.

A crucial benefit of direct injection becomes apparent from the boost pressure demand. As the density of hydrogen with  $0.08 \text{ kg/m}^3$  at normal conditions is the lowest among gaseous fuels, the subsequent displacement of air in the intake runner leads to a significantly lower volumetric efficiency when injecting while the intake valve is open [18]. This results in a boost pressure demand that

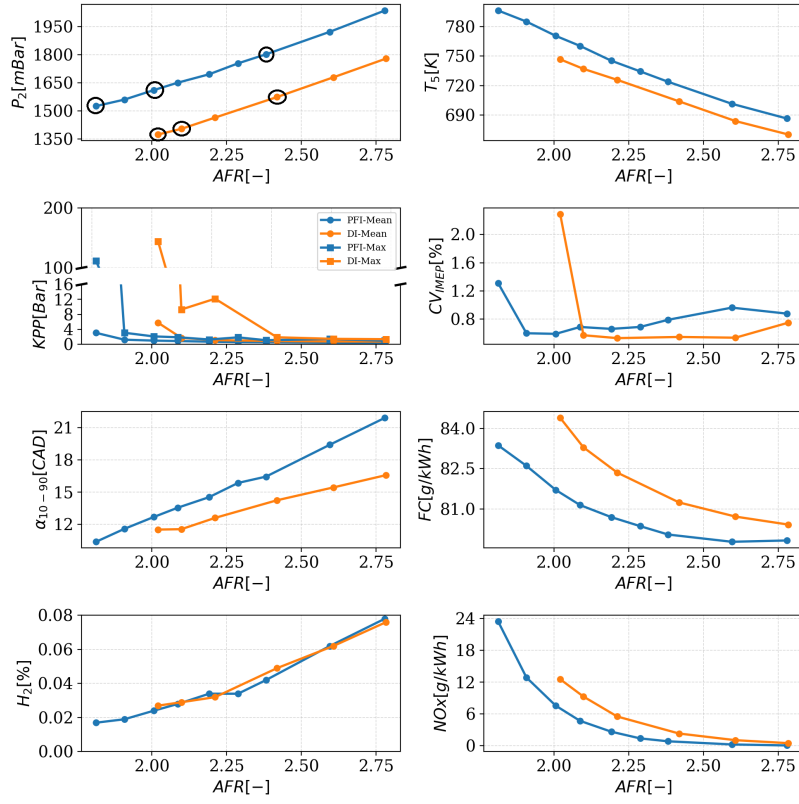


Figure 4: Experimental results of the AFR variation with the PFI and DI configurations. Black circles highlight the operating points that are numerically simulated.

is approximately 15 % higher than with the direct injection variant. Consequently, as  $p_5$  was adjusted to be equal to  $p_2$ , the exhaust temperature is higher for the PFI configuration due to the less significant expansion.

The filtered knock amplitude from peak to peak (KPP) is used to examine the knock behaviour of the engine. In the diagram, the average and maximum values of the recorded 200 engine cycles are displayed. A base KPP value of 0.5 bar is expected due to general noise of the engine. The AFR variation is started at  $AFR = 2.8$ . Afterwards, the AFR is enriched until the knock limitation is reached. In this case, the limitation is defined by a maximum KPP value of 20 bar. The results show that there is a sharp knock limit at an AFR of 2.0 for DI and 1.8 for PFI operation. In those measurements, at least one knock event of  $KPP > 100$  bar occurs and stable operation is not possible without compromising the integrity of the engine. It can be concluded that the knock tendency is impacted by the mixture homogeneity.

An indication for the combustion stability is the coefficient of variation (CV) of the IMEP. The stability limit is defined as  $CV_{IMEP} = 3$  %. Apart from the sudden increase at rich AFR due to knocking, an increasing trend for leaner mixtures is evident. For premixed combustion systems, the flame kernel development is directly influenced by the local AFR of the mixture in the proximity of the spark plug. This influences the shape of the heat release rate to a great extent. Therefore, as the cyclic fluctuation of the local AFR increase, the combustion stability decreases. Even at an AFR of 2.8, the  $CV_{IMEP}$  remains below 1 %. Therefore, the wide flammability range of hydrogen allows for a very stable combustion even for lean mixtures as the mixture can be ignited reliably.

A fast burn rate has a positive impact on the engine efficiency, as the combustion timing gets closer to the ideal Otto cycle. On the other hand, fast combustion leads to higher temperatures during combustion and therefore promotes the formation of NOx and increased wall heat losses. Even though the mixture homogenization of the PFI configuration is better than with the DI configuration, the DI combustion burns at a higher rate. Due to the injection directly into the cylinder the mixture has less time to homogenize and thus is

225 stratified. Consequently, as it will be shown in Sec. 4.4, the rich zones close to  
the spark plug burn faster.

The results for the fuel consumption (FC) display an overall lower fuel con-  
sumption for the PFI configuration. This difference is even more apparent at  
low AFR due to knocking tendencies under these conditions. The DI configu-  
230 ration has the benefits of lower compression work and higher combustion speed  
and the charge composition can be assumed almost equal. Therefore, the wall  
heat losses must be further investigated to determine the cause of the difference  
in efficiency, as hydrogen tends to have a high wall heat transfer compared to  
other fuels [37]. Hence, the in-cylinder heat transfer will be further reviewed in  
235 Sec. 4.5. By leaning the mixture even further, the reduced combustion speed  
and increasing unburnt fuel fraction predominate the benefits gained from the  
leaner mixtures.

When looking at the emissions behaviour of a hydrogen engine, two emis-  
sion components need to be investigated thoroughly. As the combustion is never  
240 ideal, a certain amount of unburnt  $H_2$  is expected during operation. High hydro-  
gen concentrations in the exhaust gas may raise safety concerns and therefore  
need to be investigated. The measurements show that leaner operation increases  
the fraction of unburnt fuel in the exhaust. This is expected from a premixed  
combustion, as the quenching distance increases with the flame thickness [38].  
245 Considering the reciprocal relation of the flame thickness to the flame speed,  
it can be inferred that the amount of unburnt hydrogen increases in leaner  
mixtures. Though, the results show that the hydrogen concentrations in the  
exhaust gas do not raise concerns for a possible after-combustion. Disregarding  
post-oxidation, the measured hydrogen content in the exhaust gas suggests a  
250 combustion efficiency of over 99 % at all investigated AFRs. NO<sub>x</sub> is the only  
significant pollutant emitted by a hydrogen engine. The results indicate that the  
NO<sub>x</sub> emissions have a significant dependency on the AFR. The lower cylinder  
charge mass causes higher overall temperatures which contributes to the NO<sub>x</sub>  
formation. Moreover, the effect of the mixture homogenization can be deduced  
255 from the NO<sub>x</sub> emissions, as rich zones lead to a faster combustion and higher

temperatures, and thus to higher NOx emissions. Therefore, the PFI configuration, which has an almost homogeneous mixture shows significantly lower emissions.

It becomes apparent that the optimum AFR is a trade-off between thermal efficiency, emissions, boost pressure demand and exhaust gas temperature. Engines without exhaust gas after-treatment systems will need to operate with very lean mixtures. Contrarily, engines with after-treatment systems need a lower AFR to keep the catalysts at working temperature.

*Ignition sweep.* Other than the AFR, the ignition timing can heavily influence the engine operation and therefore needs to be optimized to improve the thermal efficiency and emission behaviour. In the previous AFR variation it was shown that at a AFR of 2.4 stable operation in the cruise point was realized. The following ignition sweep was performed in the same operating point and the AFR is kept constant at that value.

In Fig. 5, the results of the ignition sweeps with both configurations are shown. Here, the values are displayed over the COC. Due to the efficiency loss at later ignition timings, the boost pressure demand increases to keep the AFR constant. Considering the results from the AFR variation, the differences of the intake pressure  $p_2$  and exhaust temperature  $T_5$  between DI and PFI configuration are as expected.

The KPP values indicate that in this operating point, no knocking occurs even at advanced spark timings. On the other hand, the combustion stability is reduced with retarded ignition timing. Still, the defined stability limit of  $CV_{IMEP} = 3\%$  is not reached throughout the measurement. The combustion duration increases with late ignition timings due to the higher burning distance and lower temperature during compression. This, combined with the fact that the center of combustion moves further away from the optimal timing of around 7 CADaTDC impacts the fuel consumption negatively. A minimum fuel consumption of 79.6 g/kWh for the PFI configuration is measured. The energy consumption is therefore approximately 17% higher compared to a state of the

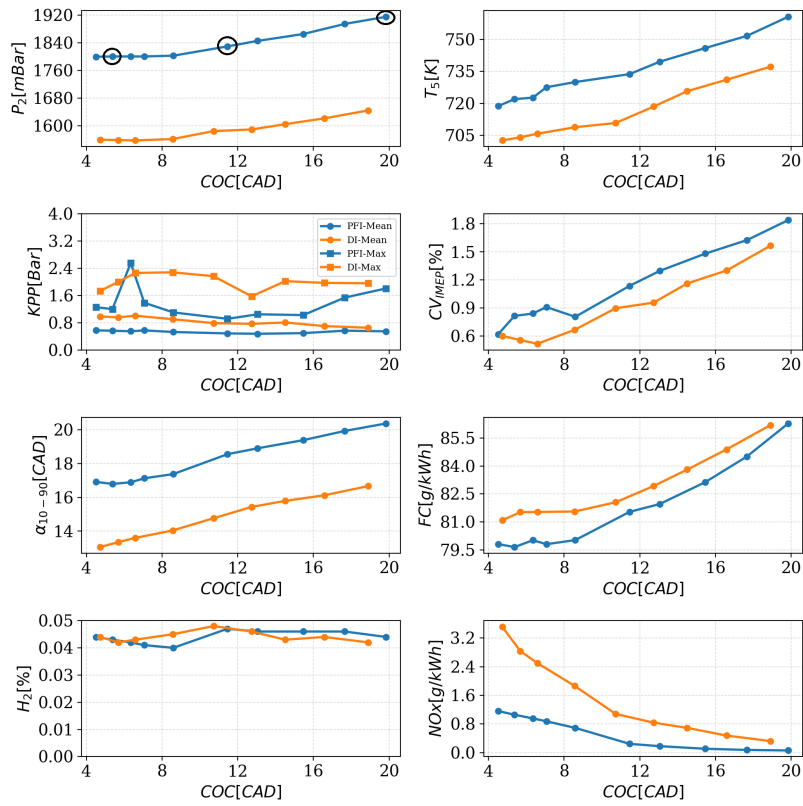


Figure 5: Experimental results of the ignition sweep with the PFI and DI configurations at fixed Air/Fuel ratio. Black circles highlight the operating points that are numerically simulated.

art diesel engine of the same class [36]. Considering the optimization potential of the hydrogen engine, further improvement of the efficiency can be expected. The plateau of lowest fuel consumption is rather large, allowing for some margin when choosing an optimized ignition timing.

290 The emissions measurement shows that the  $H_2$ -slip is not influenced by the ignition timing, so an increase of post-oxidation of the fuel due to the higher exhaust gas temperatures can be disregarded. The NOx emissions on the other hand increase when the ignition is advanced as the peak temperatures increase significantly. It can be concluded that retarded ignition timings are a viable  
295 strategy to increase the exhaust temperature and reduce NOx emissions with no major impact on the stability. The lean operating strategy allows for engine-out NOx emissions below 1 g/kWh, reducing the effort regarding the aftertreatment system compared to diesel engines. This will result in a positive impact on the overall economy of the system.

### 300 **3. Numerical modelling strategy**

CONVERGE<sup>TM</sup> V3.0 3D CFD solver [39] is used in the present work to conduct the numerical simulations. In the RANS CFD numerical framework, the RNG  $k$ - $\varepsilon$  turbulence model [40] is chosen to close the sub-grid Reynolds stress tensor. To model the turbulence-chemistry interaction in stratified premixed  
305 flame conditions the Extended Coherent Flame Model (ECFM) [27] is used. The fundamental elements of such a turbulent combustion model are shortly presented below, including the choice of the thermo-chemistry database that is used to generate the required look-up tables. In addition, in the Appendix section, a validation test case is also performed to apriori verify the modeling  
310 approach before moving to the fired engine simulations.

#### *3.1. ECFM TKI model*

The ECFM turbulent combustion model [27] accounts for the propagation of a stratified premixed flame front in the flamelet regime [41]. It describes the

flame as a geometrical surface evolving in the turbulent flow field. In ECFM-  
 315 RANS formalism [27] the mean reaction rate due to flame propagation  $\dot{\omega}_c^\Sigma$  is  
 expressed as  $\overline{\rho_u} S_l \Sigma$  where  $\overline{\rho_u}$  is the Reynolds averaged density in the fresh gases,  
 $S_l$  the unstretched laminar flame speed (tabulated from a look-up table) and  
 $\Sigma$  the local flame surface density (the flame surface per unit of volume). The  
 flame surface density is computed solving the following transport equation:

$$\frac{\partial \Sigma}{\partial t} + \frac{\partial \tilde{u}_i \Sigma}{\partial x_i} = \frac{\partial}{\partial x} \left( \frac{1}{\tilde{\rho}} \left( \frac{\mu_t}{Sc_t} + \frac{\mu}{Sc} \right) \frac{\partial \Sigma}{\partial x_i} \right) + (P_1 + P_2 + P_3 + P_4) \Sigma - D + P_k \quad (1)$$

320 Where  $\tilde{u}_i$  is the Favre averaged mean  $i^{th}$  velocity component,  $\mu$  and  $\mu_t$  the lam-  
 inar and turbulent viscosity and  $Sc$  and  $Sc_t$  the laminar and turbulent Schmidt  
 number. In this work  $Sc$  and  $Sc_t$  are both set equal to 0.78. The source and  
 sink terms  $P_1$ ,  $P_2$ ,  $P_3$ ,  $P_4$ ,  $D$  and  $P_k$  are modelled according to the closure  
 proposed in [27] and [34]. In particular, the term  $P_1 = \alpha_{ECFM} \Gamma_k \Sigma$  represents  
 325 the flame surface production by turbulent stretch. Here, the efficiency function  
 $\Gamma_k$  is computed using the formulation proposed by Bougrine *et al.* [42]. The  
 modeling constant  $\alpha_{ECFM}$  allows controlling the turbulent flame speed.

In the ECFM model the  $S_l$  tabulation reproduces the global reaction rate  
 and consequently the flame heat release rate. Differently from the previous  
 330 work [34], the laminar flame speed is tabulated, for the complete set of mixture  
 (equivalence ratio) and thermodynamic (temperature and pressure) properties  
 encountered in engine conditions, from 1D unstretched freely propagating flame  
 computations. In ECFM, balance equations for species present in unburned  
 and burned gases are used. The mean progress variable  $\tilde{c}$  is deduced from these  
 335 species mass fractions as explained in [43]. Its source term is closed as follows:

$$\tilde{\omega}_c = (1 - \tilde{c}_{ai}) (\dot{\omega}_c^\Sigma + \dot{\omega}_c^{ign}) + (1 - \tilde{c}_\Sigma) \dot{\omega}_c^{ai} \quad (2)$$

where  $\tilde{c}_\Sigma$  and  $\tilde{c}_{ai}$  are the flame propagation and auto-ignition progress vari-  
 ables, respectively. The auto-ignition source term  $\dot{\omega}_c^{ai}$  is closed according with  
 the latest version of the Tabulated Kinetics of Ignition (TKI) model [43] tabu-  
 lating the progress variable reaction rate  $\dot{\omega}_c^{ai}$  as a function of the local progress  
 340 of ignition  $c_{ai}$  for homogeneous constant pressure reactors.

$\dot{\omega}_c^{ign}$  accounts for the energy deposition due to the spark ignition and is computed according to the Imposed Stretch Spark Ignition Model (ISSIM) [31].

The choice of the thermo-chemistry database, used to compute the unstretched freely propagating flame speed and the constant pressure reactors  
345 to build-up the look-up tables for flame speed and auto-ignition trajectories, will be discussed in the next section.

In past ECFM simulations, simplified chemistry was used in the burned gases zone [43] where  $O_2$ ,  $N_2$ ,  $H_2O$ ,  $H$ ,  $O$ ,  $OH$ ,  $N$  are assumed at equilibrium and fuel oxidation is represented by two steps involving  $CO$ ,  $CO_2$  and  $H_2O$  as products.  
350 With this approach, NOx emissions were modeled using the Zeldovitch mechanism coupled to these reactions. In the present simulations, it was found that NOx were strongly under-predicted with this simplified model. For this reason, a more accurate method, developed at IFPEN in CONVERGE, was used: the simplified chemistry in the burned gases is replaced by the SAGE chemical  
355 solver employing any chemical mechanism chosen by the user. For the present simulations, the Polimi  $H_2$  mechanism [44] was selected because it includes a well validated NOx sub-set mechanism [45]. This modelling approach avoids to make equilibrium and steady-state assumptions to compute  $O$ ,  $OH$  and  $N$  radicals, and includes additional routes to NOx formation that are not accounted  
360 in the Zeldovitch mechanism. The post-flame ECFM-SAGE model adds a moderate extra-CPU cost since it is limited only at the combustion phase when the post-flame detailed chemistry calculation is activated.

### 3.2. Thermo-chemistry database

In order to generate the look-up table necessary for the 3D engine calculations  
365 a preliminary chemical kinetic study was conducted. To develop combustion-based technologies for hydrogen utilization, it is essential to acquire a good understanding of the detailed kinetics processes taking place with  $H_2$ . Estimation of global combustion properties such as auto-ignition delay and laminar flame speed are available in the literature for hydrogen, but for a range  
370 of pressures, temperatures and equivalence ratios that don't cover those of an

engine, especially for the laminar flame speed. To mitigate this lack of experimental data, kinetic uncertainties are assessed by comparing different literature kinetic mechanisms at engine conditions. The main characteristics (number of species and reactions) of each mechanism are shown in Tab. 2.

Table 2: Kinetic mechanisms apriori compared for the choice of the one to use in 3D simulation. For each mechanism the number of species and reactions are specified in the table.

Mechanisms	Species	Reactions
Aramco [46]	581	3037
PoliMi [47]	21	62
Glarborg [48]	68	631
MACDIL [49]	22	102
LLNL [50]	1389	5935
Varga [51]	15	44

375 Figure 6 shows the comparison between ignition delay times computed with the different mechanisms and the experiments from Keromnés *et al.* [52]. The measurements are performed in a shock tube at 32 atm and at lean conditions. At  $\lambda = 2.0$ , globally all mechanisms follow the experimental trend, but the best agreement is obtained by LLNL and MACDIL mechanisms. Figure 6 shows  
380 also the comparison between laminar flame speed simulation results with the selected mechanisms and the measurements from Konnov *et al.* [53]. Laminar burning velocity measurements are performed for  $H_2$ /air mixtures at 1 atm and 300 K. At these conditions, all mechanisms predict similar flame speeds in good agreement with the experiment. Note that the Aramco mechanism could not  
385 be converged for  $\lambda < 2.0$ . For both  $IDT$  and  $S_l$ , numerical comparisons were also conducted at higher pressure and for different mixture conditions, achieving similar conclusions. Considering ignition delay and laminar flame speed results together with the size of the available mechanisms, the MACDIL one is retained to generate the look-up tables necessary for ECFM turbulent combustion model.

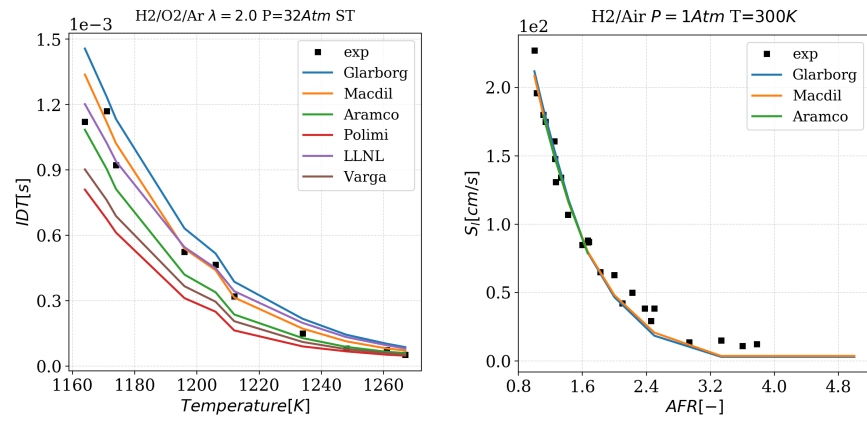


Figure 6: Left figure: comparison between 0D constant pressure simulation results with the selected mechanisms and the measurements from Keromn s et al. [52] for ignition delay times. Measurements are performed in shock tube considering a  $H_2/O_2/Ar$  mixture at lean condition  $\phi = 0.5$  and  $p = 32$  atm . Lines, simulation; symbols, measurement. Right figure: comparison between freely propagating flame simulation results with the selected mechanisms and the measurements from Konnov et al. [53] for laminar burning velocities of  $H_2/air$  mixtures at  $p = 1$  atm pressure and an initial temperature of  $T = 300$  K.

## 390 4. 3D simulation of the engine configuration

Before running 3D-CFD combustion simulation, the coupling between the ECFM-TKI model and the generated look-up tables is validated for the auto-ignition prediction in an academic configuration considering a 3D closed homogeneous vessel as shown in the Appendix.

### 395 4.1. Computation strategy

Among the experimental data points shown in the previous section, only a sub-set of them is selected for the CFD computations. Firstly, to validate the 3D-CFD modelling approach the homogeneous PFI points are simulated. In a second step, the validated model is used to compute the DI points that  
400 involve more complex phenomena such as the H<sub>2</sub>/Air mixture stratification. Table 3 summarizes the ensemble of the nine experimental points that are here considered for the numerical study indicating also for each of them the spark advance (SA) and the global AFR. The computed points include a:

- PFI-IS (Ignition Sweep): three PFI points on the experimental ignition  
405 sweep shown in Fig. 5, at constant Air/Fuel ratio ( $\lambda = 2.4$ )
- PFI-AFRV (Air/Fuel Ratio Variation): three PFI points on the Air/Fuel ratio experimental variation, shown in Fig. 4
- DI-AFRV: three DI points on the mean Air/Fuel ratio experimental variation, shown in Fig. 4

410 As the RANS approach is used, it is possible to simulate only the mean phase averaged cycle [41]. For each operating point two cycles are systematically computed: the first one is discarded and used only to initialize the thermal and aerodynamic field for the second one.

### 4.2. Computational grid and boundary conditions

415 The computational grid is controlled in CONVERGE V3.0 combining embedding strategy and adaptive mesh refinement (AMR) using a sub-grid scale

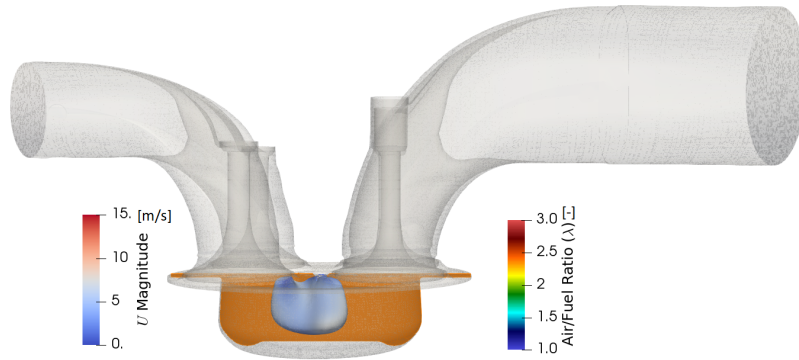
Table 3: Experimental operating points that are considered in the numerical study. For each Measured Point (MP) the Spark Advance (SA) and the global Air/Fuel Ratio (AFR) are also indicated in the table.

PFI-IS	SA	AFR	PFI-AFRV	SA	AFR	DI-AFRV	SA	AFR
PFI-MP3	18.2	2.4	PFI-MP4	16.8	2.4	DI-MP3	10.6	2.4
PFI-MP9	13.4	2.4	PFI-MP7	12.6	2.1	DI-MP5	8.1	2.1
PFI-MP15	7.3	2.4	PFI-MP10	8.8	1.8	DI-MP6	6.3	2.0

criterion based on velocity, temperature,  $H_2$  mass fraction and flame surface density. The mesh size is bounded between 0.25 and 4 mm. The combination of embedding zones and AMR allows to locally refine the computational grid and to improve consequently the resolution only in the zones where the higher gradients are located. During the different engine strokes the cell number is bounded between 0.5M and 2.5M. Regarding intake and exhaust boundary conditions, the experimental pressure and temperature signals are imposed at the location where the measurements are available in the intake and exhaust ports, respectively. To reproduce the exact position of the pressure transducer, the intake port length is 50 mm shorter for the DI configuration with respect to the PFI one as shown in Figure 7.

For intake and exhaust pressures a time-varying signal along the cycle is imposed while for temperature a constant value is retained. Exact pressure and temperature values vary depending on the operating point. Constant wall temperatures are set for the different engine parts. These values are estimated from an in-house 0D model depending on the engine load and speed; consequently, they are kept constant for all the operating points that are computed in this work. The spark advance is set equal to the experimental one (Tab. 3) for all the operating points. In the experimental test bench, the  $H_2$  injection is performed with an injector plugged within a guiding cap volume having a single hole. To simplify the 3D modelling of the injection line and to mitigate the CPU cost of the calculation, only the injection cap is included in the engine

PFI-MP4 CAD= 0



DI-MP3 CAD= 0

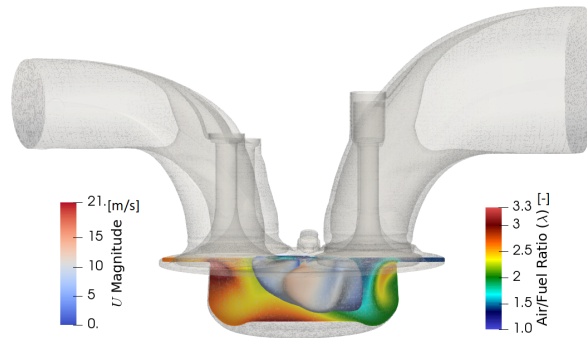


Figure 7: 3D computational geometry for the PFI-MP4 operating point (upper figure) and for the DI-MP3 one (lower figure). A 3D flame iso-surface ( $c=0.8$ ) coloured by the velocity magnitude and the 2D spark plane coloured by  $\lambda$  are also depicted in the figures. For the DI configuration the injector cap is also displayed.

simulation. However, to derive the cap inlet boundary conditions (mass flow  
 440 rate and temperature) a separate 3D simulation of the whole injection system  
 (injector and cap) was conducted. The turbulent H<sub>2</sub> jet issuing the guiding cap  
 and going into the chamber is simulated in the current CFD engine calcula-  
 tion and it is considered to be the most important phenomenon affecting the  
 in-cylinder aerodynamic field. It is expected that, as the guiding cap creates a  
 445 high pressure stagnation volume, the turbulence generated by the cap jet into  
 the cylinder weakly depends from the upstream turbulence produced inside the  
 injector volume. The cap injection surface measures 27 mm<sup>2</sup> and the injected  
 mass flow rate is 8.5E-3 kg/s at 292 K temperature. For the PFI computations,  
 the intake manifold injection process is not modelled and the intake mixture is  
 450 considered perfectly premixed at the target Air/Fuel ratio.

### 4.3. PFI configuration

For the PFI configuration, to evaluate the robustness and limitations of the  
 turbulent combustion model, two parametric variations are performed as shown  
 in Tab. 3: an ignition sweep (PFI-IS) at fixed Air/Fuel ratio and an Air/Fuel  
 455 ratio variation (PFI-AFRV).

#### 4.3.1. Ignition sweep (PFI-IS)

Three spark advance values (SA=18.2, 13.4, 7.3) are considered at  $\lambda = 2.4$   
 as shown in Tab. 3. The parameter  $\alpha_{ECFM}^{Ref}$  is calibrated on the operating point  
 PFI-MP3 and kept constant for the other ones.

460 Figure 8 shows the comparison between the numerical phase averaged cylin-  
 der pressure and the experimental one for the computed points. Despite minor  
 discrepancies are observed in the plot, the CFD model is able to correctly re-  
 produce the sensitivity to the spark advance variation in terms of pressure slope  
 and pressure peak using a unique model calibration.

#### 465 4.3.2. Air/Fuel ratio variation (PFI-AFRV)

For the PFI configuration an Air/Fuel ratio variation is performed consid-  
 ering the three points in Tab. 3. The target  $\lambda$  varies between 2.4 and 1.8.

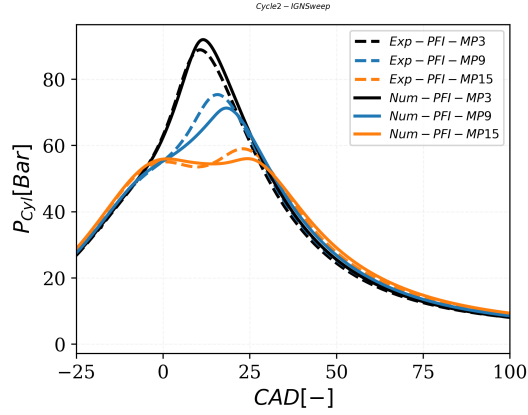


Figure 8: Comparison between the experimental and numerical in-cylinder pressure for the PFI-IS.

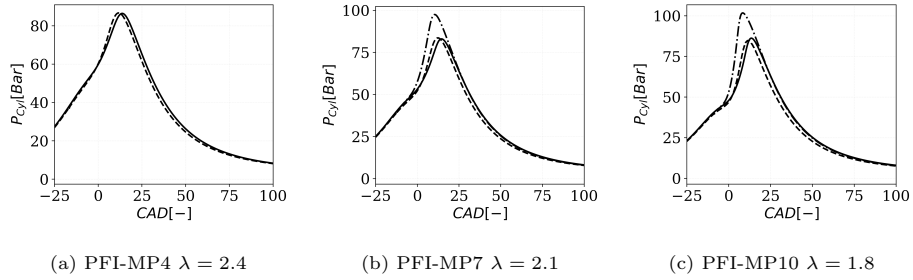


Figure 9: Comparison between the experimental and numerical in-cylinder pressure for the PFI-AFRV. The plots, differently from the ignition sweep are separated to be more readable. Dashed line: experimental data. Continuous line: numerical results using  $\alpha_{ECFM}$  re-calibration. Dashed dotted line: numerical results using  $\alpha_{ECFM} = \alpha_{ECFM}^{Ref}$ .

Figure 9 compares the mean cylinder pressures obtained in the numerical simulations with the experimental ones. Regarding the turbulent combustion model set-up, unlike from the ignition sweep, a slight re-calibration of  $\alpha_{ECFM}$  is needed to match the results with the experiments:  $\alpha_{ECFM} = \alpha_{ECFM}^{Ref}$  for  $\lambda = 2.4$ ,  $\alpha_{ECFM} = 0.75 * \alpha_{ECFM}^{Ref}$  for  $\lambda = 2.1$  and  $\alpha_{ECFM} = 0.67 * \alpha_{ECFM}^{Ref}$  for  $\lambda = 1.8$ . Such re-calibration as function of the equivalence ratio was not necessary in previous studies with ECFM using gasoline as a fuel and the reason is explained below.

The numerical pressure compares well with the experimental one except for a slight delay on the peak pressure. A systematic overestimation of the trapped mass (around 2 %) is observed for the three points which explains the overestimation of the pressure at the end of the expansion stroke. In Fig. 9, for  $\lambda = 2.1$  and for  $\lambda = 1.8$ , the results using  $\alpha_{ECFM} = \alpha_{ECFM}^{Ref}$  are also shown for comparison purposes. The need for a re-calibration of the turbulent combustion model as a function of  $\lambda$  is attributed to the absence of a differential diffusion model in ECFM and this phenomenon is particularly important for  $H_2$  to retrieve the sensitivity to flame stretch. Indeed, as  $\lambda$  increases, the Markstein length of the  $H_2$  mixture becomes more and more negative. This is due to the fact that the Lewis number is smaller than unity for  $H_2$  [54, 55]. Differently from gasoline-like spark ignition engines, where the Markstein effect is moderate as usually they operate near stoichiometric conditions, for  $H_2$  fuelled engines the Markstein effect is expected to be significant especially because they operate extra-lean conditions where the flame speed is boosted by such phenomenon. As shown in the review of Lipatnikov and Chomiak [56], many experimental and DNS studies showed that for a fixed laminar flame speed, the turbulent flame speed increases with the decrease of the Markstein length as in the hydrogen case. As the Markstein effect is not modeled in the current RANS-ECFM, it needs to be compensated by an increase of the turbulent strain through parameter  $\alpha_{ECFM}$  when increasing  $\lambda$ .

Recently [57], it has been shown that to account for this Markstein effect in a lean gasoline SI engine, one solution is to describe the effect of stretch on the

laminar flame speed at the resolved level, using a specific ECFM-LES model. It  
500 is though not clear whether this approach is sufficient for  $H_2$  combustion.

#### 4.3.3. Knocking analysis

The experimental analysis on the KPP parameter in Fig. 4 points out that the DI configuration reaches the knocking limit earlier (at higher AFR) than PFI. The two knocking points of the experimental AFR variation matrix are  
505 here considered. The PFI-MP10 and the DI-MP6 are identified as knocking points on the basis of the KPP index analysis (Fig. 4). However, in the RANS approach, only the mean phase averaged cycle is computed while knocking is visible on the complete pressure envelope and affects only the extreme cycles. As already shown in the literature [58, 59], when using RANS based models, only  
510 the knocking tendency can be reproduced changing the spark advance to mimic the extreme knocking cycles of the experimental envelope. In this work, the capability of the proposed RANS model to reproduce the knocking tendency is evaluated considering two engine parameters: the global percentage of the total fuel mass that is burning in auto-ignition mode and the local 3D auto-ignition  
515 index (*AI\_Index*) defined on the basis of the auto-ignition progress variable according to Eq. (2). As shown in Fig. 10, the tendency toward knocking is retrieved bringing the RANS mean cycle toward the knocking experimental cycles by progressively increasing ST. At ST=SA-7 CAD for PFI-MP10 and ST=SA-11 CAD for DI-MP6, a breakthrough point is found and the percentage  
520 of the total fuel mass burning in auto-ignition mode increases above 1% which is considered as the knocking threshold in numerical engine simulations. It is worth to notice that a more important modification of the spark advance is found in the DI-MP6 point to get the rapid increase of the auto-ignition combustion mode. This is attributed to the difficulty to exactly reproduce the  
525 engine mixture distribution as the auto-ignition delay is strongly sensitive to the AFR. Indeed, in previous numerical studies that compare RANS mixture distribution with experimental one in  $H_2$  engines, it was already pointed out that RANS results can show slight discrepancies compared with experimental

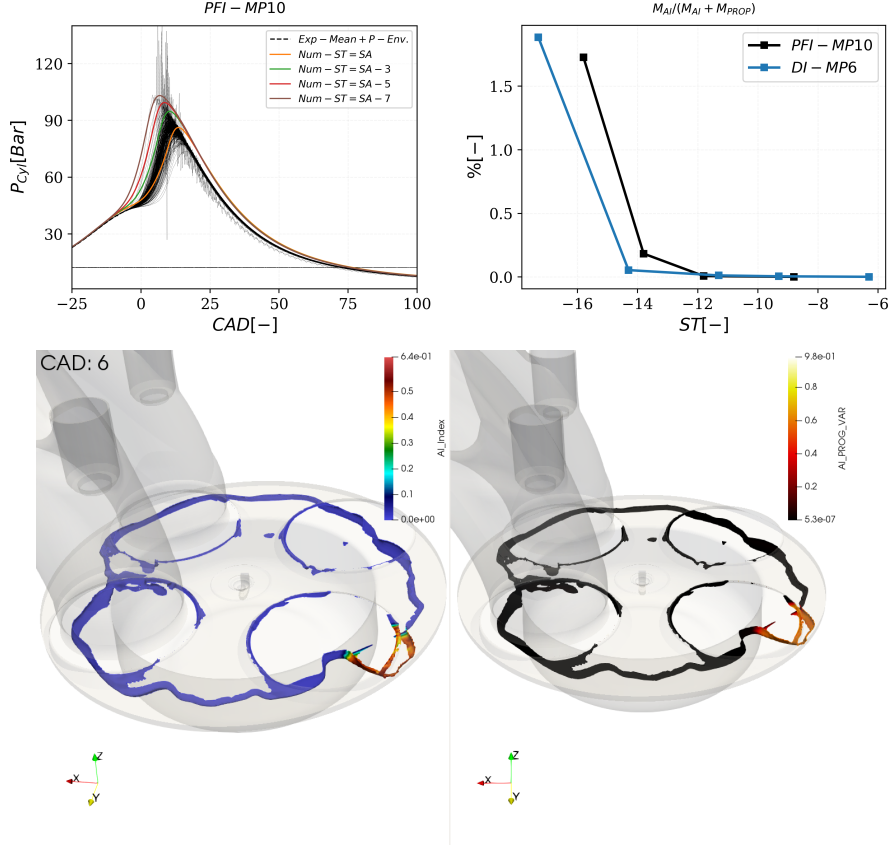


Figure 10: PFI-MP10 and DI-MP6 knocking points analysis. Upper left 1D plot: for PFI-MP10 point, experimental pressure envelope over 200 cycles compared with RANS mean phase averaged cycle for different Spark Timing (ST): SA (Experimental Spark Advance), SA-3CAD, SA-5CAD, SA-7CAD. Upper right 1D plot: evolution of the global percentage of the total fuel mass that is burning in auto-ignition mode, for PFI-MP10 and DI-MP6 points, versus the ST with respect to the Combustion TDC

. Lower 3D figure: 3D visualization of the flame iso-surface at 1800K and 6CAD for the SA-7CAD PFI-MP10 simulation case. The flame surface is coloured by the auto-ignition progress variable on the right and by the auto-ignition index [32] on the left. The intake port are also depicted in the 3D image on the left to emphasize that the auto-ignition event occurs on the exhaust side.

distribution [60] and that only with a LES approach a finer resolution of the  
530 turbulent scales can be achieved to solve the local mixing structures [61]. For  
PFI-MP10 point, at SA=RSA-7 CAD, a complementary 3D analysis is also  
conducted. Figure 10 shows, over a flame iso-surface, the auto-ignition progress  
variable and the auto-ignition index ( $AI\_Index = \tilde{c}_{ai} * (1 - \tilde{c}_{\Sigma})$ ) computed  
according to the formulation proposed in [32] to locally highlight the relative  
535 importance of the auto-ignition combustion mode with respect to the flame  
propagation mode. In the figure, it is possible to identify auto-ignition spots  
close to the exhaust seats and valves, showing a high value of the  $AI\_Index$ ;  
this denotes that the majority of fresh gases burn in auto-ignition mode in that  
zone. Such spots can be at the origin of the knocking events observed in the  
540 experiments.

#### 4.3.4. *NOx emissions prediction*

To predict NOx emissions, ECFM is employed using a detailed chemical  
mechanism in the burned gases as explained in Sec. 3. With this approach,  
only NOx emissions formed behind the flame are accounted for, while rapid  
545 NOx paths like prompt NO are not considered.

Figure 11 shows, for the PFI-AFRV, the comparison between experiments  
and simulations for NO and NO<sub>2</sub> concentrations in the exhaust gases. Although  
the correct trend with AFR is retrieved by simulations, NO is under-predicted  
by a factor between 2 and 3 approximately while NO<sub>2</sub> by a factor between 2 and  
550 5. This could be caused by the limitation of the NOx description mentioned  
above. It is worth noting that increasing  $\lambda$  from 1.8 to 2.5 NO and NO<sub>2</sub> emissions  
decrease by more than one order of magnitude, which confirms how the AFR is  
a key parameter to mitigate NOx emissions.

#### 4.4. *DI Points: DI-AFRV*

555 The same validated combustion modelling approach used for PFI studies is  
here used to compute the DI points indicated in Tab. 3. The scope of this  
analysis is to understand the in-cylinder phenomena that could suggest future

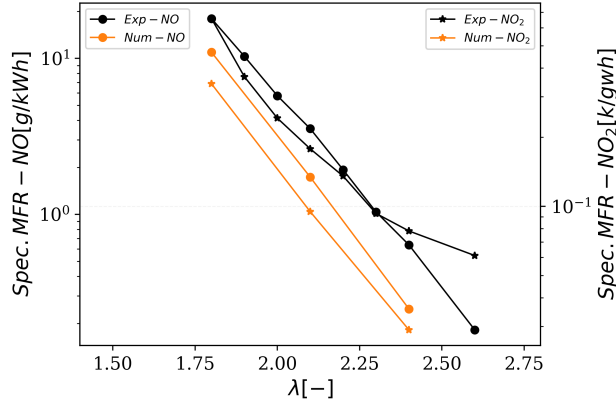


Figure 11: NO and NO<sub>2</sub> exhaust gases emissions (specific NO and NO<sub>2</sub> mass flow) from experiment and numerical simulations for the PFI points. Experimental data is shown for the all the PFI operating points considered in the  $\lambda$  sweep (Fig. 4) while for the simulation the three PFI-AFRV variation points are considered (Tab. 3).

improvements of the engine design. For the three points the mean  $\lambda$  varies from 2.4 to 2.0. A unique value is retained for  $\alpha_{ECFM}$  for the three points and equal to  $\alpha_{ECFM}^{Ref}$  used in the PFI simulations.

Figure 12 shows the evolution of the in-cylinder pressure for the three DI points. The results show a good agreement with experiments for DI-MP3 and DI-MP5 operating points but for DI-MP6 point the turbulent combustion velocity is overestimated. This is in accordance with the observation made in the

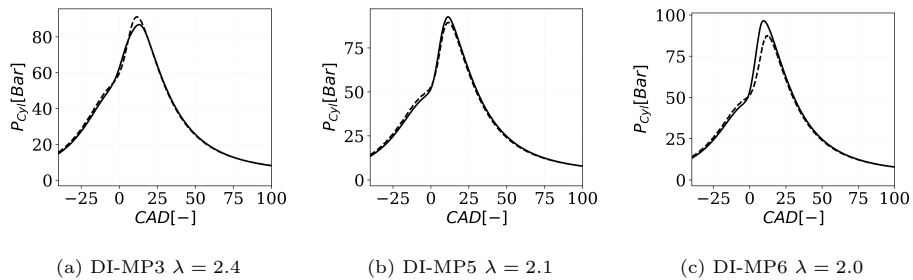


Figure 12: Comparison between the experimental and numerical in-cylinder pressure for the DI-AFRV. Dashed line: experimental data. Continuous line: numerical results.

565 PFI-AFRV study. Indeed, using a unique  $\alpha_{ECFM} = \alpha_{ECFM}^{Ref}$  leads to an overes-  
 timation of the combustion speed for the richer points. However, compared to  
 PFI points, the overestimation is mitigated because the direct in-cylinder H<sub>2</sub>  
 injection induces a similar mixture stratification profile for all the operating points  
 as shown in Fig. 13 where, comparing the DI-MP3 at mean  $\lambda = 2.4$  and DI-MP5  
 570 at mean  $\lambda = 2.0$ , a similar mixture distribution is observed: a rich spot close  
 to the spark plug and a progressively leaner mixture going toward the cylinder  
 walls. The spark-plug rich spot accelerates the combustion speed with respect to  
 the corresponding PFI points (same mean  $\lambda$ ) as supported by the experimental  
 study in Fig. 4 looking to the combustion duration ( $\alpha_{10-90}$ ). This conclusion is  
 575 also visible in Fig. 7 where, for the DI-MP3 point, mixture stratification makes  
 the flame propagate faster and that, despite for PFI-MP4 the spark advance  
 is larger than DI-MP3 one, at the combustion top dead center, the 3D flame  
 surface and burning rate are larger for the DI case. Furthermore, Fig. 13 shows  
 that the local rich spot increases the temperature and consequently promotes  
 580 NO and NO<sub>2</sub> formation which have longer time scale compared to flame surface.

#### 4.5. PFI-MP4 and DI-MP3 heat transfer analysis

In the experimental study it was observed that, for the cruise point investi-  
 gated in this work, the direct H<sub>2</sub> injection does not allow to increase the global  
 engine efficiency (FC in Fig. 4 and 5), which was attributed to wall heat losses  
 585 contribution. To support this experimental observation, wall heat losses for the  
 PFI-MP4 and DI-MP3 points, characterized by the same mean AFR=2.4, are  
 further investigated. The 3D integrated wall heat losses are computed for the  
 PFI-MP4 and DI-MP3 points splitting the contribution of the different cylinder  
 boundary walls. The integration is conducted for the whole combustion phase:  
 590 from the spark timing to the end of the combustion stroke. Table 4 summarizes  
 the comparison between the total heat losses ratio for the PFI and DI cases,  
 respectively. It is possible to observe that, for the DI case, the calculated wall  
 heat losses are higher with respect to the PFI case by about 0.6% compared  
 to the total energy introduced in the cylinder. The mixture stratification along

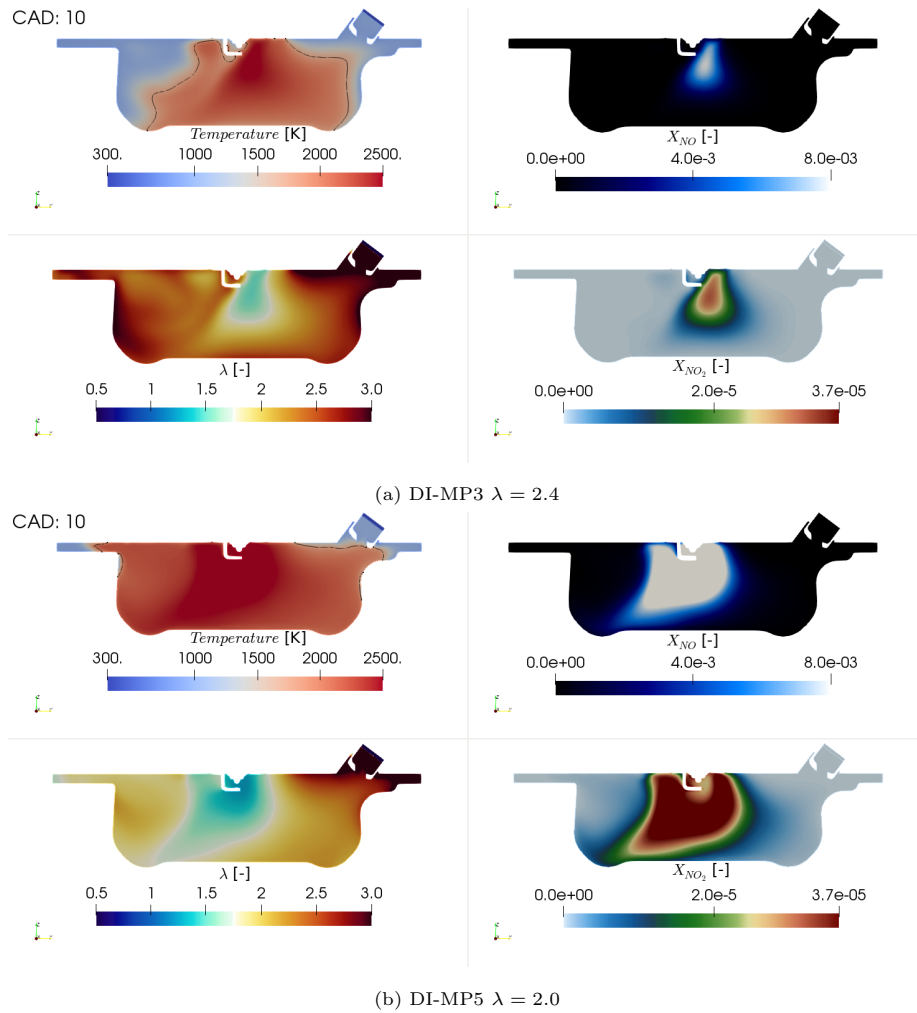


Figure 13: Colormap on the spark mid-plane at CAD=10 from the CDC, for DI-MP3 and DI-MP5 of the following quantities: Temperature,  $\lambda$ , NO and NO<sub>2</sub> formation. On the temperature map a flame iso-contour is also shown deduced by a iso-surface at progress variable=0.8

Table 4: Summary of the heat losses for the PFI-MP4 and DI-MP3 cases integrated from the spark time to the to the end of the expansion stroke. The Total Heat Losses (THL) and the ratio between THL and the Total energy introduced in the cylinder (TE) are also shown. The contribution of each cylinder part is also given: Piston (PHL), Liner (LHL) and Head (HHL). For the DI case, valves bottom contribution and injection cap one are added to the head part.

Config.	THL [J]	THL/TE [%]	PHL [%]	LHL [%]	HHL [%]
PFI-MP4 $\lambda=2.4$	4.78E+02	9.19	46.3	25.7	28.1
DI-MP3 $\lambda=2.4$	5.13E+02	9.78	47.7	25.4	26.9

595 the flame front induces higher temperature and hence higher heat losses in the DI case. This analysis corroborates the efficiency difference observed in the experimental analysis on the fuel consumption.

## Conclusions

Experiments have been conducted on a hydrogen-fueled heavy-duty SCE  
600 comparing PFI to DI strategies. The results have shown that the mixture preparation plays a key role in improving the performance and emissions of a H<sub>2</sub>-DI engine. Moreover, the thermal efficiency and emissions benefits versus the disadvantages in boost pressure demand and exhaust gas temperature from leanment have been discussed. Furthermore, an ignition sweep was performed  
605 to provide a base for validating the numerical investigations.

A 3D RANS ECFM approach was used to account for the main phenomena encountered in H<sub>2</sub> engines: spark ignition, flame propagation, auto-ignition and NO<sub>x</sub> formation. The model was successfully validated in PFI conditions with a slight re-calibration of the turbulent strain source term for richer operating  
610 conditions, which was made necessary due to the absence of preferential diffusion description in the present model. Knocking and NO<sub>x</sub> experimental tendencies were well retrieved. On the basis of the obtained results, some future research routes were also given to improve the 3D modeling approach for H<sub>2</sub> internal combustion engine. In particular, to achieve a finer turbulent flame description,

615 it will be beneficial to introduce:

- differential diffusion modelling to account for the increase of the flame surface with the increase of  $\lambda$ , that leads to negative Markstein lengths,
  - LES turbulence-flame modeling to improve mixing and knocking prediction (maximum pressure peaks and knock frequency) accounting for cycle-to-cycle variability.
- 620

On the engine design side, the joint experimental and numerical study allowed to understand that for the DI engine solution, despite the advantages in boost pressure demand with respect to the PFI configuration, efforts need to be made in the future to optimize the mixture formation and reduce wall heat losses to reach the best efficiency. To achieve this goal, future H<sub>2</sub> engine designs need to give consideration to the in-cylinder aerodynamic motion prescription (relying on tumble or swirled solutions) and its interaction with the H<sub>2</sub> direct injection jet to optimize the mixture formation.

625

### Acknowledgements

630 This project has received funding from the European Union’s Horizon 2020 research and innovation programme under Grant Agreement no. 874972

### References

- [1] G. A. Karim, Hydrogen as a spark ignition engine fuel, *International Journal of Hydrogen Energy* 28 (2003) 569–577.
  - 635 [2] Iea (2021), global hydrogen review 2021, iea, paris, 2021. URL: <https://www.iea.org/reports/global-hydrogen-review-2021>.
  - [3] M. Pein, N. C. Neumann, L. J. Venstrom, J. Vieten, M. Roeb, C. Sattler, Two-step thermochemical electrolysis: An approach for green hydrogen production, *International Journal of Hydrogen Energy* 46 (2021) 24909–24918.
- 640

- [4] G. Kakoulaki, I. Kougias, N. Taylor, F. Dolci, J. Moya, A. Jäger-Waldau, Green hydrogen in europe—a regional assessment: Substituting existing production with electrolysis powered by renewables, *Energy Conversion and Management* 228 (2021) 113649.
- 645 [5] J. E. Lee, K.-J. Jeon, P. L. Show, S.-C. Jung, Y. J. Choi, G. H. Rhee, K.-Y. A. Lin, Y.-K. Park, et al., Mini review on h2 production from electrochemical water splitting according to special nanostructured morphology of electrocatalysts, *Fuel* 308 (2022) 122048.
- [6] M. Yu, K. Wang, H. Vredenburg, Insights into low-carbon hydrogen production methods: Green, blue and aqua hydrogen, *International Journal of Hydrogen Energy* 46 (2021) 21261–21273.
- 650 [7] M. H. A. Khan, R. Daiyan, P. Neal, N. Haque, I. MacGill, R. Amal, A framework for assessing economics of blue hydrogen production from steam methane reforming using carbon capture storage & utilisation, *International Journal of Hydrogen Energy* 46 (2021) 22685–22706.
- 655 [8] M. Ramadan, A review on coupling green sources to green storage (g2g): case study on solar-hydrogen coupling, *International Journal of Hydrogen Energy* 46 (2021) 30547–30558.
- [9] J. C. Beziat, R. Edwards, J. F. Larivé, Well-to-wheels analysis of future automotive fuels and powertrains in the european context, version 4.a, Joint Research Center of the European Commission, Eucar (2014).
- 660 [10] European Commission, A hydrogen strategy for a climate-neutral europe (2020).
- [11] H. Fayaz, R. Saidur, N. Razali, F. Anuar, A. Saleman, M. Islam, An overview of hydrogen as a vehicle fuel, *Renewable and Sustainable Energy Reviews* 16 (2012) 5511–5528.
- 665 [12] A. Ajanovic, A. Glatt, R. Haas, Prospects and impediments for hydrogen fuel cell buses, *Energy* 235 (2021) 121340.

- [13] X. Liu, K. Reddi, A. Elgowainy, H. Lohse-Busch, M. Wang, N. Rustagi,  
670 Comparison of well-to-wheels energy use and emissions of a hydrogen fuel  
cell electric vehicle relative to a conventional gasoline-powered internal com-  
bustion engine vehicle, *International Journal of Hydrogen Energy* 45 (2020)  
972–983.
- [14] S. Verhelst, Recent progress in the use of hydrogen as a fuel for internal  
675 combustion engines, *international journal of hydrogen energy* 39 (2014)  
1071–1085.
- [15] G. Frenette, D. Forthoffer, Economic & commercial viability of hydrogen  
fuel cell vehicles from an automotive manufacturer perspective, *International  
Journal of Hydrogen Energy* 34 (2009) 3578–3588.
- 680 [16] G. Reverdiau, A. Le Duigou, T. Alleau, T. Aribart, C. Dugast, T. Priem,  
Will there be enough platinum for a large deployment of fuel cell electric  
vehicles?, *International Journal of Hydrogen Energy* 46 (2021) 39195–  
39207.
- [17] C. Acar, I. Dincer, The potential role of hydrogen as a sustainable trans-  
685 portation fuel to combat global warming, *International Journal of Hydro-  
gen Energy* 45 (2020) 3396–3406.
- [18] S. Verhelst, T. Wallner, Hydrogen-fueled internal combustion engines,  
*Progress in Energy and Combustion Science* 35 (2009) 490–527.
- [19] C. White, R. Steeper, A. Lutz, The hydrogen-fueled internal combustion  
690 engine: a technical review, *International Journal of Hydrogen Energy* 33  
(2006) 1292–1305.
- [20] J. Liu, C. E. Dumitrescu, 3d cfd simulation of a ci engine converted to si  
natural gas operation using the g-equation, *Fuel* 232 (2018) 833–844.
- [21] O. Laget, S. Richard, D. Serrano, D. Soleri, Combining experimental and  
695 numerical investigations to explore the potential of downsized engines op-

erating with methane/hydrogen blends, *International journal of hydrogen energy* 37 (2012) 11514–11530.

- [22] R. Babayev, A. Andersson, A. S. Dalmau, H. G. Im, B. Johansson, Computational characterization of hydrogen direct injection and nonpremixed  
700 combustion in a compression-ignition engine, *International Journal of Hydrogen Energy* 46 (2021) 18678–18696.
- [23] C. Park, C. Kim, Y. Choi, S. Won, Y. Moriyoshi, The influences of hydrogen on the performance and emission characteristics of a heavy duty natural gas engine, *International Journal of Hydrogen Energy* 36 (2011) 3739–3745.
- [24] C. Park, C. Kim, Y. Choi, Power output characteristics of hydrogen-natural  
705 gas blend fuel engine at different compression ratios, *International Journal of Hydrogen Energy* 37 (2012) 8681–8687.
- [25] S. Sterlepper, M. Fischer, J. Claßen, V. Huth, S. Pischinger, Concepts for hydrogen internal combustion engines and their implications on the exhaust  
710 gas aftertreatment system, *Energies* 14 (2021) 8166.
- [26] F. M. et al., Operation principles for hydrogen spark ignited direct injection engines for passenger car applications, *International Journal of Hydrogen Energy* 47 (2022) 5638–5649.
- [27] O. Colin, A. Benkenida, C. Angelberger, 3d modeling of mixing, ignition  
715 and combustion phenomena in highly stratified gasoline engines, *Oil & gas science and technology* 58 (2003) 47–62.
- [28] S. Richard, O. Colin, O. Vermorel, A. Benkenida, C. Angelberger, D. Veynante, Towards large eddy simulation of combustion in spark ignition engines, *Proc. of the Combust. Inst.* 31 (2007) 3059–3066.
- [29] O. Colin, S. Chevillard, J. Bohbot, P. Senecal, E. Pomraning, M. Wang,  
720 Development of a species-based extended coherent flamelet model (sb-ecfm)

for gasoline direct injection engine (gdi) simulations, in: Internal Combustion Engine Division Fall Technical Conference, volume 51999, American Society of Mechanical Engineers, 2018, p. V002T06A016.

- 725 [30] A. J. Sai, R. Balamurugan, C. Servant, F. Ravet, S. A. Kumar, Applying ecfm combustion model to spark ignition engine, comparison with experimental data, in: *Advances in Fluid and Thermal Engineering*, Springer, 2019, pp. 729–741.
- [31] O. Colin, K. Truffin, A spark ignition model for large eddy simulation based on an fsd transport equation (issim-les), *Proceedings of the Combustion Institute* 33 (2011) 3097–3104.
- 730 [32] A. Robert, S. Richard, O. Colin, L. Martinez, L. De Francqueville, Les prediction and analysis of knocking combustion in a spark ignition engine, *Proceedings of the Combustion Institute* 35 (2015) 2941–2948.
- [33] D. Aubagnac-Karkar, J.-B. Michel, O. Colin, P. E. Vervisch-Kljakic, N. Darabiha, Sectional soot model coupled to tabulated chemistry for diesel rans simulations, *Combustion and Flame* 162 (2015) 3081–3099.
- 735 [34] V. Knop, A. Benkenida, S. Jay, O. Colin, Modelling of combustion and nitrogen oxide formation in hydrogen-fuelled internal combustion engines within a 3d cfd code, *International Journal of Hydrogen Energy* 33 (2008) 5083–5097.
- 740 [35] R. Ono, M. Nifuku, S. Fujiwara, S. Horiguchi, T. Oda, Minimum ignition energy of hydrogen–air mixture: Effects of humidity and spark duration, *Journal of Electrostatics* 65 (2007) 87–93.
- 745 [36] H.-O. Herrmann, A. Gorbach, H. Lettmann, E. Chebli, Die (R)evolution der Daimler Heavy Duty Engine Plattform, *37th International Vienna Motor Symposium* (2016) 370–384.

- [37] J. Demuynck, M. De Paepe, I. Verhaert, S. Verhelst, Heat loss comparison between hydrogen, methane, gasoline and methanol in a spark-ignition internal combustion engine, *Energy Procedia* 29 (2012) 138–146.
- 750 [38] D. Suckart, D. Linse, E. Schutting, H. Eichlseder, Experimental and simulative investigation of flame–wall interactions and quenching in spark-ignition engines, *Automotive and Engine Technology* 2 (2017) 25–38.
- [39] K. J. Richards, P. K. Senecal, E. Pomraning, *Converge (v3.0)*, Convergent Science, Madison, WI 19 (2016).
- 755 [40] Z. Han, R. D. Reitz, Turbulence modeling of internal combustion engines using rng  $\kappa$ - $\varepsilon$  models, *Combustion science and technology* 106 (1995) 267–295.
- [41] T. Poinso, D. Veynante, *Theoretical and numerical combustion*, RT Edwards, Inc., 2005.
- 760 [42] S. Bougrine, S. Richard, O. Colin, D. Veynante, Fuel composition effects on flame stretch in turbulent premixed combustion: Numerical analysis of flame-vortex interaction and formulation of a new efficiency function, *Flow, turbulence and combustion* 93 (2014) 259–281.
- 765 [43] O. Colin, S. Chevillard, J. Bohbot, P. K. Senecal, E. Pomraning, M. Wang, Development of a Species-Based Extended Coherent Flamelet Model (SB-ECFM) for Gasoline Direct Injection Engine (GDI) Simulations Volume 2: Emissions Control Systems; Instrumentation, Controls, and Hybrids; Numerical Simulation; Engine Design and Mechanical Development (2018).
- 770 [44] E. Ranzi, A. Frassoldati, A. Stagni, M. Pelucchi, A. Cuoci, T. Faravelli, Reduced kinetic schemes of complex reaction systems: fossil and biomass-derived transportation fuels, *International Journal of Chemical Kinetics* 46 (2014) 512–542.
- [45] Y. Song, L. Marrodán, N. Vin, O. Herbinet, E. Assaf, C. Fittschen, A. Stagni, T. Faravelli, M. Alzueta, F. Battin-Leclerc, The sensitizing
- 775

effects of no<sub>2</sub> and no on methane low temperature oxidation in a jet stirred reactor, *Proceedings of the Combustion Institute* 37 (2019) 667–675.

- 780 [46] C.-W. Zhou, Y. Li, U. Burke, C. Banyon, K. P. Somers, S. Ding, S. Khan, J. W. Hargis, T. Sikes, O. Mathieu, et al., An experimental and chemical kinetic modeling study of 1, 3-butadiene combustion: Ignition delay time and laminar flame speed measurements, *Combustion and Flame* 197 (2018) 423–438.
- 785 [47] E. Ranzi, A. Frassoldati, R. Grana, A. Cuoci, T. Faravelli, A. Kelley, C. K. Law, Hierarchical and comparative kinetic modeling of laminar flame speeds of hydrocarbon and oxygenated fuels, *Progress in Energy and Combustion Science* 38 (2012) 468–501.
- [48] H. Hashemi, J. M. Christensen, S. Gersen, P. Glarborg, Hydrogen oxidation at high pressure and intermediate temperatures: Experiments and kinetic modeling, *Proceedings of the Combustion Institute* 35 (2015) 553–560.
- 790 [49] B. Xu, Multi-Scale Kinetic Modeling of Highly-Diluted Gasoline Premixed Flames, Ph.D. thesis, 2019.
- [50] M. Mehl, W. J. Pitz, C. K. Westbrook, H. J. Curran, Kinetic modeling of gasoline surrogate components and mixtures under engine conditions, *Proceedings of the Combustion Institute* 33 (2011) 193–200.
- 795 [51] T. Varga, C. Olm, T. Nagy, I. G. Zsély, É. Valkó, R. Pálvölgyi, H. J. Curran, T. Turányi, Development of a joint hydrogen and syngas combustion mechanism based on an optimization approach, *International journal of chemical kinetics* 48 (2016) 407–422.
- 800 [52] A. Kéromnès, W. K. Metcalfe, K. A. Heufer, N. Donohoe, A. K. Das, C.-J. Sung, J. Herzler, C. Naumann, P. Griebel, O. Mathieu, et al., An experimental and detailed chemical kinetic modeling study of hydrogen and syngas mixture oxidation at elevated pressures, *Combustion and Flame* 160 (2013) 995–1011.

- [53] A. A. Konnov, A. Mohammad, V. R. Kishore, N. I. Kim, C. Prathap,  
805 S. Kumar, A comprehensive review of measurements and data analysis  
of laminar burning velocities for various fuel+ air mixtures, *Progress in  
Energy and Combustion Science* 68 (2018) 197–267.
- [54] J. Beeckmann, R. Hesse, S. Kruse, A. Berens, N. Peters, H. Pitsch, M. Mat-  
alon, Propagation speed and stability of spherically expanding hydro-  
810 gen/air flames: Experimental study and asymptotics, *Proceedings of the  
Combustion Institute* 36 (2017) 1531–1538.
- [55] E. Varea, J. Beeckmann, H. Pitsch, Z. Chen, B. Renou, Determination of  
burning velocities from spherically expanding h<sub>2</sub>/air flames, *Proceedings  
of the Combustion Institute* 35 (2015) 711–719.
- 815 [56] A. Lipatnikov, J. Chomiak, Molecular transport effects on turbulent flame  
propagation and structure, *Progress in Energy and Combustion Science* 31  
(2005) 1–73.
- [57] O. Benoit, K. Truffin, S. Jay, J. van Oijen, Y. Drouvin, T. Kayashima,  
P. Adomeit, C. Angelberger, Development of a large-eddy simulation  
820 methodology for the analysis of cycle-to-cycle combustion variability of a  
lean burn engine, *Flow, Turbulence and Combustion* (2021) 1–40.
- [58] C. Netzer, L. Seidel, F. Ravet, F. Mauss, Assessment of the validity of  
rans knock prediction using the resonance theory, *International Journal of  
Engine Research* 21 (2020) 610–621.
- 825 [59] A. d’Adamo, S. Breda, F. Berni, S. Fontanesi, The potential of statistical  
rans to predict knock tendency: Comparison with les and experiments on  
a spark-ignition engine, *Applied Energy* 249 (2019) 126–142.
- [60] R. Scarcelli, T. Wallner, N. Matthias, V. Salazar, S. Kaiser, Mixture  
830 formation in direct injection hydrogen engines: Cfd and optical analysis  
of single-and multi-hole nozzles, *SAE International Journal of Engines* 4  
(2011) 2361–2375.

- [61] J. Le Moine, P. Senecal, S. A. Kaiser, V. M. Salazar, J. W. Anders, K. Svensson, C. Gehrke, A computational study of the mixture preparation in a direct-injection hydrogen engine, *Journal of Engineering for Gas Turbines and Power* 137 (2015).

835